Single particle entropy stability and the temperature-entropy diagram in quantum dot transistors

Faris Abualnaja,[1] Wenkun He ●,[1] Aleksey Andreev ●,[2] Mervyn Jones,[1] and Zahid Durrani ●[1,*]

[1]*Department of Electrical and Electronic Engineering, Imperial College London, South Kensington, London SW7 2AZ, United Kingdom*
[2]*A-Modelling Solutions Ltd., Forster Road, Guildford, Surrey GU2 9AE, United Kingdom*

Single and double quantum dot (QD) transistors have been used to investigate entropy transitions in the single particle limit. Precisely controlled QD electron states allow a few-particle thermodynamic system to be defined. Charge stability diagrams are calculated to find the Gibbs entropy S vs bias voltage, providing a framework to define single particle entropy diagrams. The calculation method is applied to experimental dopant atom QD transistor characteristics. As multiple states become occupied, S increases in a stepwise manner towards $S = k \ln \Omega$, where Ω is the total number of microstates, retaining the Boltzmann interpretation of entropy. The T-S diagram vs gate voltage, where T is temperature, reflects underlying single particle state transitions and enables the definition of heat cycles. These diagrams approximate the behavior of macroscopic phase changes in magnetic, liquid-vapor, and superconducting systems.

I. INTRODUCTION

Interpreting fundamental laws of thermodynamics, formulated historically using many particles or microstates, becomes increasingly complex at the few-particle level [1]. A well-known example is Maxwell's demon and its reduction to a single particle system by Szilard [2,3]. Here, statistical variations in particle energy lead, theoretically, to contradictions of the second law of thermodynamics. Resolving this requires careful consideration of information entropy changes [3–5]. Recently, quantum dots (QDs), which enable precise control over single electrons, have been used experimentally to realize Szilard's engine and to observe Landauer's entropy for 1 bit of information, $S = k \ln 2$ [6–11], where S is the Gibbs entropy and k is Boltzmann's constant. Energy exchange and heat cycles in quantum computation have also been analyzed using a single particle thermodynamics framework [12–15].

Semiconductor QDs and single electron transistors (SETs) [16–18] provide a tool to tunably probe thermodynamics at the single particle, microstate level. These devices control precisely the number of particles N on a QD, suggesting a method to define thermodynamic macrostates with a known number of constituent microstates. Thermodynamic parameters, e.g., energy and entropy, of small macrostates may then be probed as the number of underlying microstates is changed one by one. Single QDs and double QDs (DQDs) [17,19] have been used to investigate single particle entropy exchange

[6,10,20,21], theoretically predict spin-charge-to-charge-state phase transitions [22], build heat pumps [9,23], and propose heat engine cycles [24–26]. Single particle thermodynamics is also of great interest in understanding surface molecular dynamics [27,28] and determining fundamental limits on the minimum power consumption of integrated circuits [29]. However, S and energy changes in QD devices have yet to be mapped to their charge stability diagrams. The evolution from single particle to multiple particle, classical entropy also remains unclear. Furthermore, multiparameter T-S plots, where T is temperature, widely used in classical thermodynamics to understand phase transitions and entropy dynamics at phase boundaries and to underpin heat engines [30,31], have yet to be determined for these single particle systems.

In this paper, a method to extract S for single QD, DQD, and multi-QD systems, from zero to moderate (<10) electron number, is developed and applied to the experimental characteristics of a dopant atom DQD transistor [32]. Each electron is associated with a particle microstate such that the quantum system forms a thermodynamic macrostate with size controlled by applied bias. This provides a generalized approach to understand entropy and state transitions in single particle systems. A numerical method, applying single electron master equation simulations [33], is used to extract the Gibbs entropy S corresponding to the single and double QD transistor charge stability diagrams. Within this framework, S vs transistor bias voltages is quasi-phase-diagram-like where each constant entropy charge state is separated from neighboring states by the single electron charging energy E_c [19]. For points in the stability diagram where Ω states meet, $S/k = \ln \Omega$, Boltzmann's entropy formulation. We show that S/k is equal to $\ln 1$, $\ln 2$ (Landauer's 1-bit limit [4]), and $\ln 3$, at points where a single state, two states, and three states coexist. $S/k \rightarrow \ln \Omega$ as the number of states increases further. It is then possible to predict few-particle T-S diagrams vs gate voltage, enabling heat cycles to be
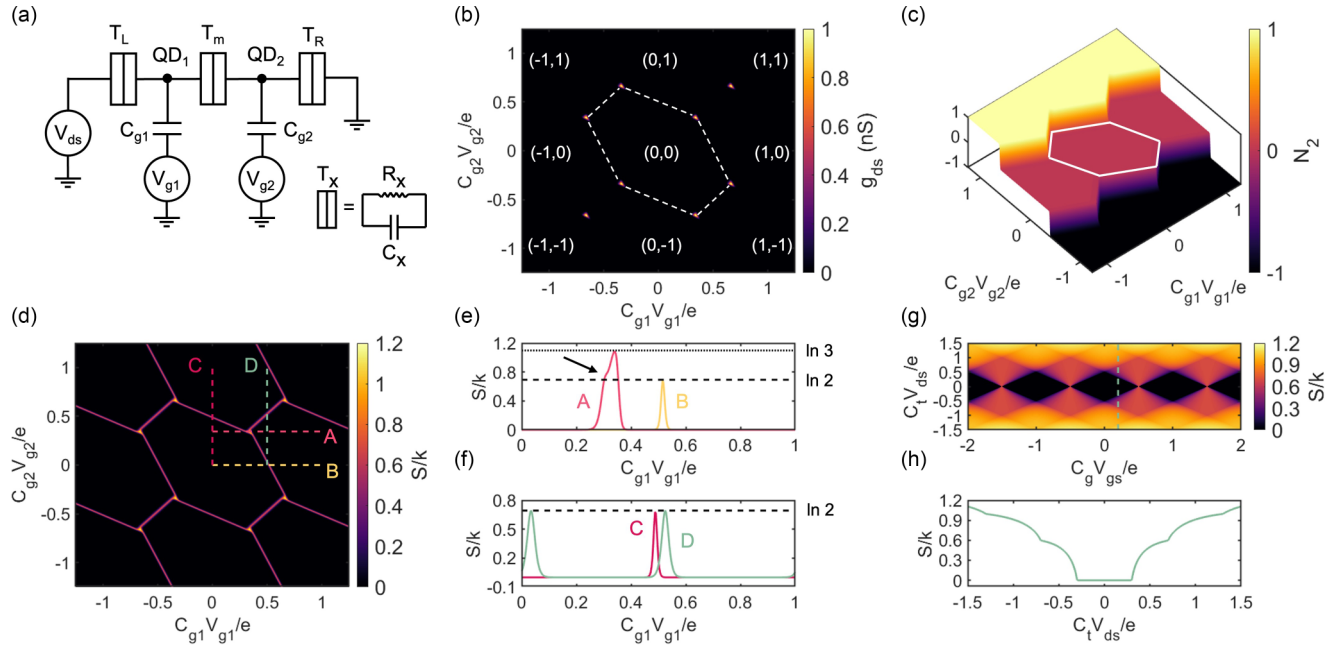
---

*z.durrani@imperial.ac.uk

FIG. 1. (a) A series DQD circuit for single electron simulation results in (b). Tunnel junctions T_x are represented as a resistor and capacitor in parallel. C_{g1} (C_{g2}) couples QD_1 (QD_2) to V_{g1} (V_{g2}). (b) DQD charge stability diagram with average additional number of electrons (N_1 and N_2) regions marked. Units are scaled to the electron charge ($C_{g1}V_{g1}/e$ and $C_{g2}V_{g2}/e$), while the conductance, g_{ds}, is normalized to the total conductance of the device. (c) N_2 on QD_2 with a hexagon charge stability region marked by a white line. (d) S/k for the DQD calculated using the results in (b) and (c). (e) Horizontal (lines A and B) and (f) vertical (lines C and D) line traces of the S/k plot in (d). (g) S/k for a single QD device with normalized axes. (h) A vertical line trace in (g) at $C_gV_{gs}/e = 0.2$ between $C_tV_{ds}/e = +1$ and $C_tV_{ds}/e = -1$.

defined. Our T-S diagrams show similarities with many-particle antiferromagnetic-paramagnetic phase diagrams vs magnetic field [34,35] and, more broadly, with phase diagrams in liquid-vapor (e.g., water-steam) [30], ferromagnetic-paramagnetic [36], and superconducting-normal systems [15]. However, while near-constant temperature regions are observed in our T-S diagrams, these show smooth, thermally activated transition edges. This differs from the observation of constant temperature regions with abrupt edges in classical multiparticle phase transitions.

II. SINGLE ELECTRON ENTROPY EXTRACTION

A. Numerical analysis

Figure 1 shows the numerical analysis results for a general series of DQD and single QD transistors. In Fig. 1(a) the DQD circuit is illustrated. When considering a single QD transistor circuit, T_m is instead connected to ground. The conductance (g_{ds}) for the DQD is shown in Fig. 1(b) with plot axes scaled to the electron charge ($C_{g1}V_{g1}/e$ and $C_{g2}V_{g2}/e$). The average additional numbers of electrons (N_1, N_2) on QD_1 and QD_2 is also marked in Fig. 1(b). These are calculated using $N_1 = \sum_{m,n} m p_{(m,n)}$ and $N_2 = \sum_{m,n} n p_{(m,n)}$. The integers m and n represent the number of electrons on QD_1 and QD_2, respectively, and $p_{(m,n)}$ is the probability that a QD is in the charge configuration (m,n), summed over all possible combinations of (m,n). Figure 1(c) shows N_2 vs $C_{g1}V_{g1}/e$ and $C_{g2}V_{g2}/e$ for QD_2 with changes in N_2 occurring along the $C_{g2}V_{g2}/e$ axis. In contrast, changes in N_1 vs $C_{g1}V_{g1}/e$ and $C_{g2}V_{g2}/e$ for QD_1 occur along the $C_{g1}V_{g1}/e$ axis; this plot is not shown.

The probabilities $p_{(m,n)}$ are found by solving the single electron master equation [33]. The N_1 and N_2 values show the dominant charge configuration (N_1, N_2) within each charge stability region, and the dominant charge configurations are the most likely values of N_1 (N_2) at given V_{g1} (V_{g2}) and V_{ds} values. To calculate the entropy S for a QD in a DQD system, we use Gibbs's entropy definition $S = -k \sum_i p_i \ln p_i$, where k is the Boltzmann constant, p_i is the probability that the system is in the charge state i, and the summation is carried over all these possible states. Furthermore, the sum of the probabilities for having i electrons on the QD is $\sum_i p_i = 1$. Therefore the entropy for each QD is $S_1 = -k \sum_i p_i^{(1)} \ln p_i^{(1)}$ and $S_2 = -k \sum_j p_j^{(2)} \ln p_j^{(2)}$, where the superscripts "(1)" and "(2)" for $p_{i(j)}$ and the subscripts "1" and "2" for S correspond to QD_1 and QD_2. The total reduced entropy (S_{tot}/k) of the system is calculated in a similar way:

$$S_{\text{tot}} = S_{1+2} = -k \sum_{i,j} p_{(i,j)} \ln p_{(i,j)}, \qquad (1)$$

where $p_{(i,j)}$ is the probability that QD_1 has i electrons and QD_2 has j electrons and the summation is carried over all possible combinations of (i, j).

B. Statistical dependence between QDs

We now consider the case that QD_1 and QD_2 are statistically independent. Here, S_{tot}/k is the same as in Eq. (1); however, since the two dots are assumed to be statistically independent, the following joint probability relation is

used:

$$p_{(i,j)} = p_i^{(1)} p_j^{(2)}. \tag{2}$$

Hence, using Eq. (2), S_{tot} from Eq. (1) may be rewritten for two independent QDs as

$$
\begin{aligned}
S_{\text{tot}} = S_{1+2} &= -k \sum_{i,j} p_{(i,j)} \ln p_{(i,j)} \\
&= -k \sum_i \sum_j p_i^{(1)} p_j^{(2)} \ln p_i^{(1)} p_j^{(2)} \\
&= -k \sum_i p_i^{(1)} \ln p_i^{(1)} + -k \sum_j p_j^{(2)} \ln p_j^{(2)} \\
&= S_1 + S_2. \tag{3}
\end{aligned}
$$

Equation (3) shows that S_{tot} for two independent QDs will be the same as the sum of entropies for each individual QD, i.e., $S_{\text{tot}} = S_1 + S_2$. However, since QD_1 and QD_2 are tunnel coupled [Fig. 1(a)], the two dots in a DQD are statistically dependent, and $S_{\text{tot}} \neq S_1 + S_2$.

C. Entropy plots

The DQD's reduced entropy, S/k, is shown in Fig. 1(d). The hexagon patterns that appear in the charge stability diagram are also present in the N_2 plot; an example of this is marked by the white hexagon in Fig. 1(c). Figures 1(e) and 1(f) show changes in S/k across hexagon boundaries for horizontal (dashed lines A and B) and vertical (dashed lines C and D) line traces in Fig. 1(d). Traces across hexagon edges in both horizontal and vertical cases show peaks with height $S/k = \ln 2$, corresponding to the two states defined by the two hexagon regions. However, when tracing across a triple point [horizontal line A in Fig. 1(d)], where three hexagon regions meet and three states are available for occupancy [(0,0), (0,1), and (1,0)], $S/k = \ln 3$. A small shoulder [arrow in Fig. 1(e)] is observed at $S/k = \ln 2$ as p_i changes from one to three probable states.

Similar S/k characteristics are observed in the charge stability diagram for a single QD device [Fig. 1(g)]. Coulomb diamonds, where no current flows, have $S/k = 0$, while boundaries and regions outside are >0. A vertical line trace between $-1 < C_t V_{ds}/e < 1$ for $C_g V_{gs}/e = 0.2$ is shown in Fig. 1(h). Here, the number of available states Ω increases as $|C_t V_{ds}/e|$ increases, resulting in $S/k \to \ln \Omega$.

The observation of $S = 0$ within each charge stability hexagon in Fig. 1(d) and, in addition, constant S diamonds in Fig. 1(g) implies that these regions may be viewed as thermodynamic states of fixed order. This has analogies to Kondo charge-spin states based on order which have been interpreted previously as phase regions [22]. Each state is separated from its neighbors by a change in energy E_c with a two-state boundary at the hexagon or Coulomb diamond edges. Triple points occur at the hexagon vertices. In a DQD, E_c corresponds to the relevant QD charging energy for (0,0)–(0,1) transitions and inter-QD coupling energy for (0,1)–(1,0) transitions. A change in energy is essential to move from one thermodynamic region to another, and at nonzero temperature the state boundary is mixed due to nonzero probability of either state.

D. Double quantum dot entropy

The DQD may be considered within a statistical mechanics picture. A full DQD macrostate can be constructed using microstates consisting of the total possible electron states on each QD. The number of significantly occupied microstates (electrons), and hence S, can then be controlled with V_{ds}, V_{g1}, V_{g2}, and T, forming a macrostate controlled by applied bias.

Figures 2(ai)–2(aiii) show S/k diagrams for a DQD at $T = 30$, 60, and 90 K, respectively. As T rises, the uncertainty in N_1 and N_2 increases, raising S/k at the boundaries and towards hexagon centers. Figure 2(b) shows S/k curves for traces along $V_{g2} = 0$ V for different temperatures, with peaks occurring when crossing hexagon boundaries. These peaks arise from the changes in electron number for adjacent hexagons [see Figs. 1(b) and 1(c)]. For lower temperatures, e.g., 30 K, these peaks are narrow with a maximum at $\ln 2$ because there are only two states available. However, at higher temperatures, these peaks broaden and their height rises to $S/k > \ln 2$. This is because, although two states are likely, other, less likely, states are also available. Minimum S/k values appear at hexagon centers, where T has a reduced effect because the Coulomb blockade effect is maximized.

Figures 2(c) and 2(d) show T vs S/k curves for points along the paths I–II and II–III, respectively, marked in Fig. 2(ai) for increasing V_{g1}. At points I and III, hexagon centers, T has a minimum effect. However, at point II, a hexagon boundary, a small rise in T shifts S/k towards a $\ln 2$ limit. A further rise in temperature sees $S/k \geqslant \ln 2$ as more states become thermally accessible. The 1-bit information limit, $\ln 2$, is also seen in experimentally observed entropy variations of a doublet state in magnetic phase transitions. These have a remarkably similar T-S diagram as a function of external magnetic field [35]. Here, the underlying physics, based on a change in order from one to two states, is the same as in our single particle system. The symmetric behavior between the paths I–II and II–III is a reflection of the hexagon patterns in the charge stability diagram. This behavior, where order changes from $S/k = 0$ to $S/k = \ln 2$ to $S/k = 0$, is analogous to (α or β)–γ–δ phase (bcc-fcc-bcc atomic configuration) ferromagnetic-paramagnetic transitions [36] (see Sec. IV). However, as our state transitions are thermally activated, abrupt edges where $d^2 T/dS^2 \to \infty$ are not observed.

III. EXPERIMENTAL ANALYSIS

The preceding method for extraction of S can be applied to experimental single electron transistor characteristics to quantify energy exchanges in nonideal experimentally fabricated devices, propose heat cycles, and estimate the corresponding efficiency. We now extract entropy plots from the experimental current-voltage (I-V) characteristics of a phosphorous (P) dopant atom DQD point-contact transistor, capable of room temperature (RT) operation.

A. Fabrication method

Dopant atom, $Si/SiO_2/Si$ point-contact QD transistors are fabricated in the heavily n-doped (P, concentration $\sim 10^{20}/\text{cm}^3$), ~ 30-nm-thick top Si layer of silicon-on-insulator (SOI) material. Device patterns are defined using
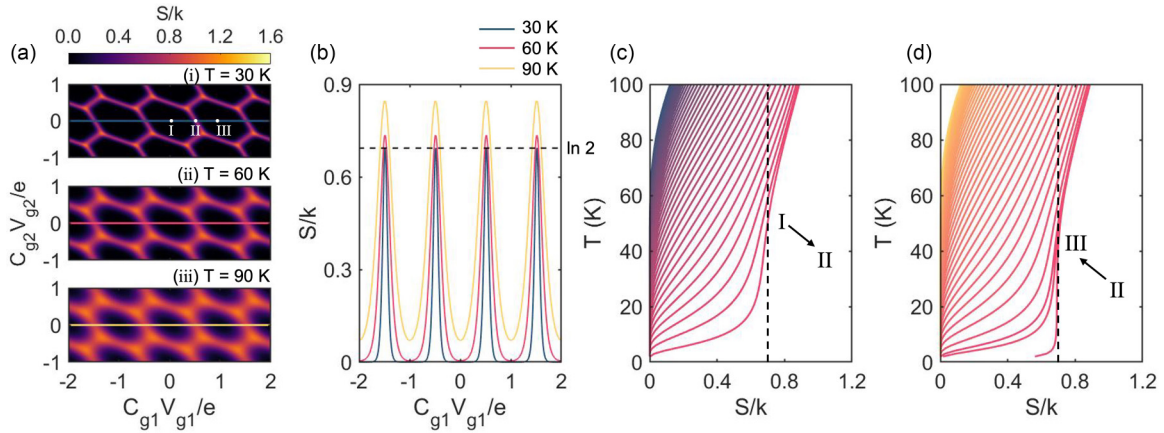
FIG. 2. (a) Temperature T dependence of S/k in a DQD device for (i) 30 K, (ii) 60 K, and (iii) 90 K. (b) Line traces at $C_{g2}V_{g2}/e = 0$ between $C_{g1}V_{g1}/e = -2$ and $C_{g1}V_{g1}/e = 2$ with maximum transitions between two states, ln 2, marked by a dashed line. (c) and (d) T-S diagrams, with $S/k = \ln 2$ marked by a dashed line, for the path from point I to point II and the path from point II to point III, respectively, marked in (ai).

high-resolution electron beam lithography in bilayer poly(methyl methacrylate) (PMMA) resist, followed by reactive-ion etching in SF_6 plasma to transfer the pattern into the top Si layer. Side gates are trench isolated from the point-contact, source, and drain regions. The device geometry is exploited to oxidize completely the approximately $10 \times 10 \times 30$-nm planar area point-contact region, trapping P dopant atom QDs within a SiO_2 tunnel barrier [20,21,32,37,38]. The QDs tunnel couple to each other and to source and drain terminal regions on either side. Side gates electrostatically control QD energy states and device current and allow tuning to single or double QD operation [32,37,38]. Tunnel barrier heights are ∼3 eV, sufficient for RT confinement of electrons on the dopant atom states [37]. Figure 3(a) shows a scanning electron micrograph (SEM) of the device, and Fig. 3(b) illustrates the device schematically.

A simplified equivalent circuit for this device is illustrated in Fig. 4(a). Here, two QDs are capacitively coupled to a single gate and are used to reproduce the electrical characteristics and identify QD coupling configurations. The device
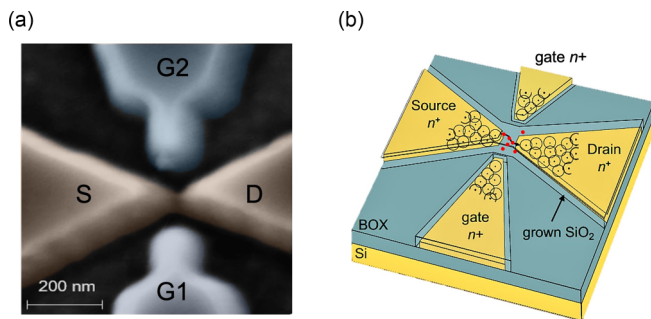

FIG. 3. (a) False-color SEM of the DQD device in SOI material. Source (S) and drain (D) terminals connect to the point contact, approximately 10×10 nm in planar area. Side gates (G1 and G2) couple capacitively to the point contact. (b) Schematic diagram of the device. Source, drain, point-contact, and gate layers are defined in the top Si layer. Geometric oxidation of the device completely oxidizes the point-contact region, isolating P dopant atom QDs (red dots). The Bohr radii (circles) of the P dopant atoms (black dots) in the device terminals overlap, such that these remain conductive

is measured using a single gate that is capacitively coupled to multiple QDs in the SiO_2 point-contact region. Figure 4(b) shows the electrical characteristics, where Coulomb current oscillations are observed. These lead to Coulomb diamonds in the charge stability diagram. While a random arrangement of QDs exists in the point-contact region, tuning the gate voltage window allows single or double QD stability regions to be identified [32,37,38].

B. Electrical measurement

Figures 4(c) and 4(d) show drain-source current I_{ds} vs drain (V_{ds}) and gate (V_{gs}) voltage characteristics for a representative device at RT = 290 K. Measurements are performed using a single gate that couples to multiple QDs. Equivalent circuit modeling is then used to reproduce electrical characteristics and identify the QD coupling configuration [see Fig. 4(a) for the equivalent circuit]. As the current level is low and near the noise threshold (∼1 pA) in our measurement, data are averaged 17 times per measurement point to reduce noise. Three Coulomb diamonds are visible in Fig. 4(c), which overlap and change in size and shape with V_{gs} due to different gate capacitances coupling to the two dominant QDs. Further changes in diamond size can occur due to changes in the potential well shape with charge [37]. For $V_{gs} > 1$ V, no further charging states exist in this device, and $I_{ds} \sim 0$ A. This is because the number of charging states in dopant atom QDs tends to be limited [37].

Figure 4(d) shows simulated I-V characteristics of the device, using equivalent circuit single electron "master equation" modeling [33,37]. Three overlapping Coulomb diamonds with changing heights are observed, qualitatively similar to the experimental results in Fig. 4(c). The characteristics correspond to Coulomb gaps $E_{c1} \approx 0.3$ eV and $E_{c2} \approx 0.24$ eV for QD_1 and QD_2, respectively [19]. Figure 4(e) shows the result for S/k for a $C_{gs2} = 2C_{gs1}$ DQD device at 10 K, similar to the RT simulation in Fig. 4(d) (see Supplemental Material [39] for a discussion regarding changes in the C_{gs1}-to-C_{gs2} ratio). Thermodynamic state boundaries extend from Coulomb diamond edges into overlapping diamond regions [an example of a boundary is marked by the white dashed lines in Fig. 4(e)]. Traces along $V_{ds} = 0$ and
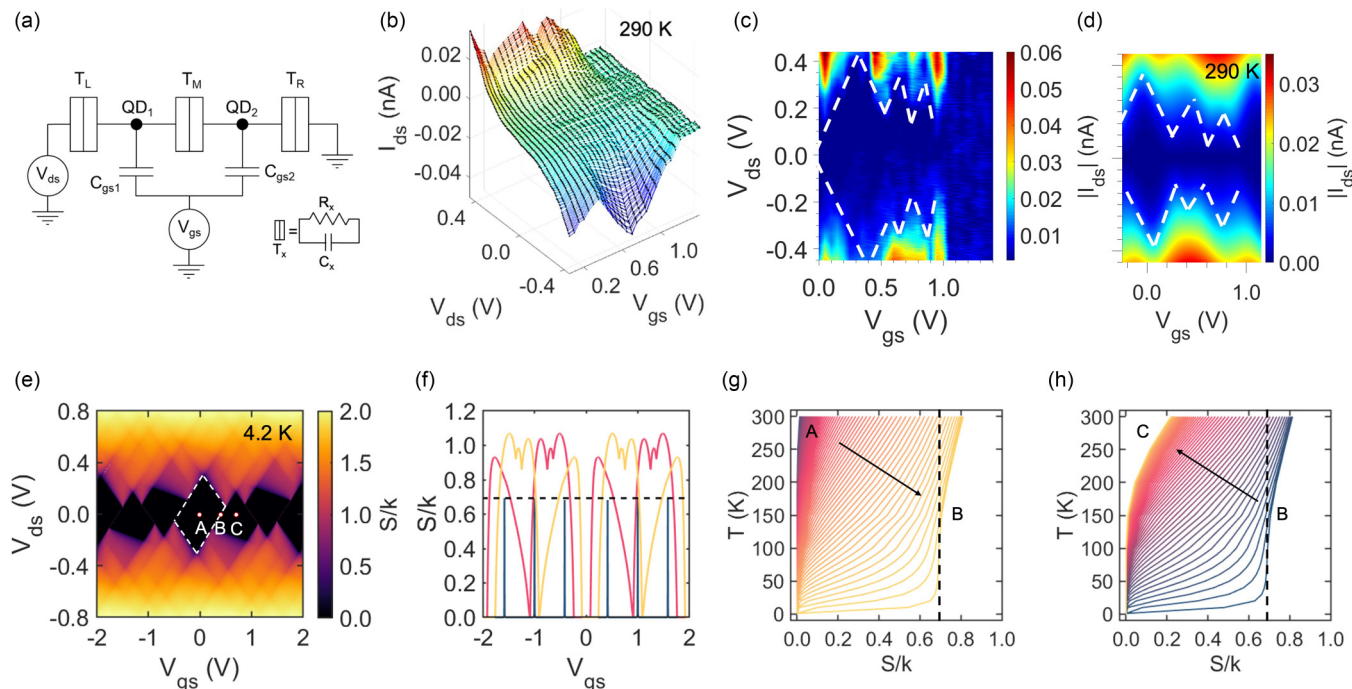
FIG. 4. (a) Equivalent circuit for DQD transistor. Tunnel junctions T_x are represented as a resistor and capacitor in parallel. C_{gs1} (C_{gs2}) couples QD_1 (QD_2) to V_{gs}. (b) I_{ds} vs V_{ds}, V_{gs} characteristics at RT = 290 K. (c) Image plot of $|I_{ds}|$ vs V_{ds}, V_{gs} characteristics at RT = 290 K. Extracted Coulomb diamond charge stability regions are marked by white dashed lines. (d) Simulation results at RT for a DQD. (e) Simulation results for a circuit configuration with different gate coupling capacitance to the two QDs ($C_{gs2} = 2C_{gs1} = 0.16$ aF), at $T = 10$ K. (f) Horizontal line scans at $V_{ds} = 0$ V (blue) and $V_{ds} = +0.2$ and -0.2 V (yellow and red, respectively) between $V_{gs} = 2$ V and $V_{gs} = -2$ V with maximum transitions between two states, with ln 2 marked by a dashed line. (g) and (h) T-S curves between points A and B and between points B and C in (e), respectively.

± 0.2 V in the S/k diagram [Fig. 4(e)] between $V_{gs} = -2$ V and $V_{gs} = 2$ V are presented in Fig. 4(f). Along the trace for $V_{ds} = 0$ V (blue curve), S/k peaks at ln 2 at Coulomb diamond boundaries, as predicted. Along traces for $V_{ds} = \pm 0.2$ V, asymmetric curves are produced, peaking at different values owing to additional available states.

C. Single electron T-S diagram

Figures 4(g) and 4(h) show T-(S/k) diagrams vs V_{gs} predicted for the experimental data in Fig. 4(c), sweeping between regions A and B and between regions B and C in Fig. 4(e), respectively. A large entropy change, $S/k = 0$ to $S/k = \ln 2$, occurs at diamond boundaries (e.g., point B) as two states become equally probable. This region is suppressed for curves with V_{gs} values closer to thermodynamic state centers. In Fig. 4(g), mixed-state behavior is observed within the area bounded by the black dashed line. Similar, though reversed behavior with increasing V_{gs} occurs in Fig. 4(h).

In the T-(S/k) plots of Figs. 4(g) and 4(h), V_{gs} has analogies to the external magnetic field in antiferromagnetic T-S diagrams and to pressure in liquid-vapor T-S diagrams [30,35] (see Sec. IV for these T-S diagrams). Unlike liquid-vapor diagrams at moderate pressure, constant T (isothermal) sections are not observed in our T-S diagrams as a nonzero slope is observed. Our T-S diagram may be used as a basis to define heat cycles, e.g., the Carnot cycle or more complex cycles such as the Rankine cycle, with a view to exploit the energy changes for a quantum heat engine (see Sec. IV for Carnot and Rankine-like cycles).

IV. DISCUSSION

The QD T-S diagrams may be compared with T-S diagrams extracted for classical multiparticle systems. The latter are often used to demonstrate phase change behavior, e.g., the liquid-vapor diagram, and define heat cycles for extraction of heat engine efficiency. While our QD T-S diagrams do not show phase change behavior where it is necessary for $dT/dS = 0$, the quasi-phase-change-like behavior we observe may be compared with liquid-vapor and antiferromagnetic-paramagnetic transitions.

A. Comparison with liquid-vapor T-S diagram

Figure 5 shows a comparison between the liquid-vapor and QD T-S diagrams. The liquid-vapor T-S diagram in Fig. 5(a) is drawn schematically for isobars with increasing pressure P [30,31,40]. Figure 5(b) shows the T-(S/k) diagram for the DQD transistor discussed in the previous section. In Fig. 5(a), for all isobars passing below the critical point A, a phase change from liquid to vapor is observed with T constant, corresponding to a two-phase changing liquid-vapor mixture. In each isobar, the width of the phase change region corresponds to the latent heat of evaporation, $\Delta Q = T\Delta S$. As P increases beyond the critical point and the corresponding critical pressure isobar passing through this point, a clear phase change region is no longer observed. Phase change regions exist only for the area below the bell-shaped red dashed line, with the left and right half boundaries of the bell defining
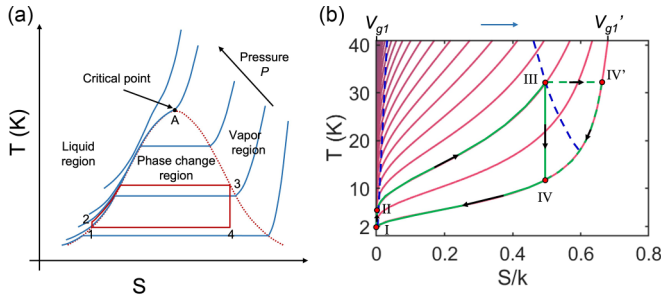
FIG. 5. (a) Schematic T-S plot of the transition between water and vapor at different pressures. The bell-shaped curve indicates the phase change region with the critical phase changing point labeled "A." The ideal Rankine thermodynamic heat cycle is also labeled (points 1–4, solid red line). (b) T-(S/k) diagram for the DQD device. A partial bell curve (blue dashed lines) is drawn to identify regions where T does not change rapidly with S. A Rankine-like cycle is indicated by the solid green curve (points I–II–III–IV–I), and a further heating-cooling cycle is indicated by the dashed green curve (points I–II–III–IV'–I).

FIG. 6. Comparison between water-steam and DQD T-S diagrams. (a) Experimental, water-to-steam, T-S diagram for phase transitions at different pressures. Data are extracted from Ref. [40]. (b) Experimentally extracted T-(S/k) diagram for the DQD transistor described in Fig. 4.

saturated liquid and saturated vapor boundaries, respectively. A superheated vapor region exists to the right of the phase change region, and a liquid region exists to the left. To the right, well away from the saturated vapor boundary, the curves obey ideal gas laws. The ideal gas Carnot cycle, consisting of two adiabatic (vertical lines on the T-S diagram) and two isothermal (horizontal lines on the T-S diagram) legs, then maps as a rectangle (not shown for clarity) onto the diagram. The solid red line in Fig. 5(a) indicates the ideal Rankine thermodynamic heat cycle, often used to describe steam turbines [30,31]. Here the phase change region is explicitly exploited in the cycle. The process from point 1 to point 2 (process 1–2) corresponds to constant S, isentropic liquid compression. Process 2–3 corresponds to heat flow to the working fluid, from liquid to saturated vapor, e.g., in the boiler of a steam turbine. Process 3–4 corresponds to isentropic expansion of the fluid, e.g., in the turbine. Process 4–1 corresponds to heat flow from the fluid at constant P and T, e.g., in the steam turbine condenser, until the saturated liquid point. The thermal efficiency for the cycle is given by $\eta = (P_t - P_p)/Q'_{in}$, where P_t and P_p are the turbine and pump power and Q'_{in} is the rate of heat transfer in the boiler. Typically, $\eta \sim 30$–40%.

The liquid-vapor T-S diagrams in Fig. 5(a) may be compared with the DQD transistor T-(S/k) diagram [Fig. 5(b)]. Here, increasing P in (a) corresponds to decreasing gate bias V_{g1} in Fig. 5(b), where $V_{g1} < V'_{g1}$. Furthermore, in Fig. 5(b) a reduced nonzero slope region occurs within the dashed blue line area. This is unlike the flat, constant T, regions in the liquid-vapor isobars and is closer to operating nearer the critical point A in the liquid-vapor diagram [Fig. 5(a)]. The reduced slope region in Fig. 5(b) also does not form a symmetrical "bell-like" shape as in Fig. 5(a), a consequence of the underlying Coulomb blockade region shapes for the DQD.

Performing a heat cycle analogous to the Rankine cycle in Fig. 5(a) for a DQD would require changing both V_{g1} and T for the isentropic, vertical legs (legs 1–2 and 3–4) in Fig. 5(b) and changing temperature, i.e., heating or cooling the DQD, to travel along a given curve for the upper and lower legs. An
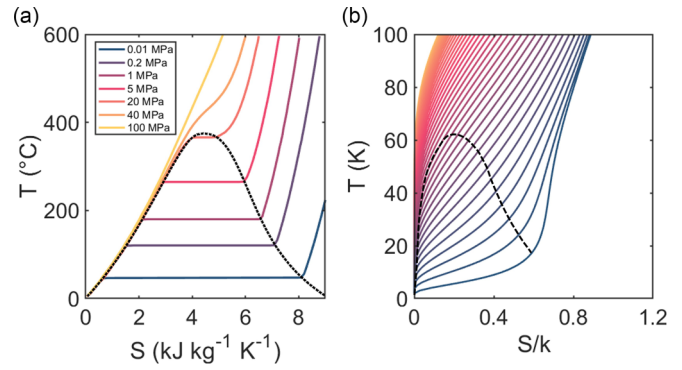
example of a Rankine-like cycle for a DQD is shown by the solid green curve, points I–II–III–IV–I, in Fig. 5(b), where the stages 1–2–3–4–1 are replaced by stages I–II–III–IV–I. This quasi-Rankine cycle does not have horizontal, isothermal, legs as in the liquid-vapor Rankine cycle in Fig. 5(a), due to the finite slopes of the curves in the quasi-phase-change area. An isothermal path in the DQD T-S diagram requires changing V_{g1} at constant T and leads to a transfer from one curve to another horizontally. During this cycle, the DQD may be used to extract heat from the environment in the leg II–III, i.e., the DQD work can potentially be used as a cooling region for nearby regions. Furthermore, change in V_{g1} from point III to point IV can in principle carry heat away from the DQD electrons, reducing electron temperature. The cycle then follows the path III–IV. If the electron remains at higher temperature at point III, then the path III–IV' is followed.

Assuming that this quasi-Rankine cycle is applicable to the DQD device, the maximum efficiency η may be calculated in an analogous manner to the liquid-vapor cycle. However, in our case, $\eta = Q_{out}/Q'_{in} = \Delta V_{g1}/(\Delta V_{g1} + kT)$, where ΔV_{g1} is the change in applied bias to gate 1 and kT is the thermal energy of the electron gained as it stays at a particular V_{g1} value. For the cycle I–II–III–IV–I presented in Fig. 5(b), an efficiency of $\eta = (0.82 - 0.78)\,\text{eV}/((0.82 - 0.78)\,\text{eV} + 8.617 \times 10^{-5}\,\text{eV K}^{-1} \times 27\,\text{K}) = 94.5\%$ is calculated. However, only a small amount of work, ~ 0.4 eV, is performed as this is extracted for only a single electron.

Another heat cycle may be designed specifically for the DQD to operate as a cooling mechanism; this is shown by the solid green curve I–II–III continuing towards the dashed green curve III–IV'–I. This process is similar to the Rankine cycle; however, at point III, instead of an isentropic process, an isothermal process takes place with an increase in V_{g1}. From point IV' to point I, the electron on the QD cools down, such that a nearby coupled system may cool.

Figure 6 compares an experimentally measured water-steam T-S diagram [Fig. 6(a)], digitally extracted from Ref. [40], and the experimentally extracted DQD T-(S/k) diagram [Fig. 6(b)]; see Fig. 4. The water-steam T-S diagram shows a phase change envelope marked by the black dashed bell curve in Fig. 6(a), where both liquid and vapor phases are
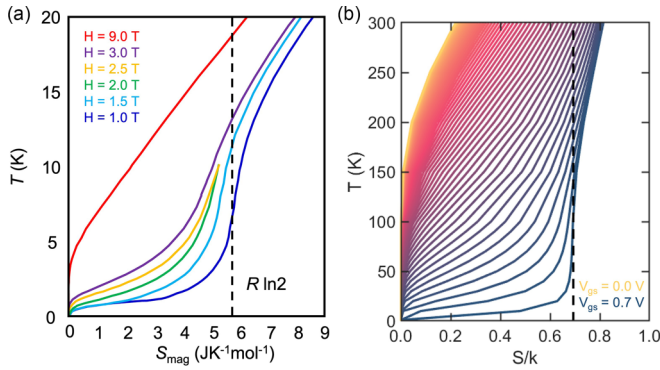
FIG. 7. (a) T-S diagram schematic for experimental phase transitions in a many-particle pyrochloric antiferromagnetic and paramagnetic material at different magnetic field strengths H (results are digitally extracted from Ref. [35]). The Landauer limit scaled by the molar gas constant $R \ln 2$ is marked by the black dashed line. (b) Experimentally extracted T-(S/k) diagram for the DQD transistor described in Fig. 4. The Landauer limit is marked by the black dashed line.

present. A similar envelope is marked in Fig. 6(b) for the DQD T-(S/k) phase diagram, where two possible electron configurations, or states, can coexist. Furthermore, in both systems, an external variable is controlled to define each T-(S/k) curve. For the water-steam case it is pressure, while for the DQD it is applied gate voltage V_{gs}.

B. Comparison with antiferromagnetic-paramagnetic T-S diagram

We also compare the experimentally extracted T-S diagram for many-particle pyrochloric antiferromagnetic and paramagnetic materials [Fig. 7(a)] with our experimentally extracted DQD T-(S/k) diagram [Fig. 7(b)]. Here we find remarkably similar T-S curve characteristics between the two systems. In the magnetic case, the T-S curve per mole in Er^{3+} has a nonzero slope, similar to those in the DQD T-S plot. Furthermore, the pressure and gate applied bias equivalent for the magnetic system is the strength of the magnetic field H. For higher magnetic fields, e.g., the red curve in Fig. 7(a),

$H = 9$ T, the system is more stable and less affected by temperature. This curve is identical to being at the center of a hexagon in the DQD entropy-stability diagram, e.g., the yellow curves in Fig. 7(b). In addition, weaker magnetic fields, e.g., the dark blue curve in Fig. 7(a), $H = 1$ T, produce a strong effect when a small change in temperature occurs. This behavior is similar to being at the boundary in our DQD diagram, e.g., the dark blue curves in Fig. 7(b). Both systems also show the Landauer limit [black dashed line in both Fig. 7(a) and Fig. 7(b)]. In Fig. 7(a) this limit is scaled to the molar gas constant $R \ln 2$, while this scaling factor is not present in Fig. 7(b). The phase transitions for the magnetic system are a result of spin alignment in the magnetic fields. The similarity arises from order found within the electronic configuration in both systems.

V. SUMMARY

Summarizing, we extract single particle entropy and thermodynamic state changes, and predict T-S diagrams, for single and double QD transistors as a function of applied bias. A numerical method, applying single electron master equation simulations, is used to calculate S vs transistor bias voltages. This defines a framework to extract entropy-stability diagrams where thermodynamic states are separated by the single electron charging energy. For points in the stability diagram where Ω states meet, $S/k = \ln \Omega$, Boltzmann's entropy formulation. We show $S/k = \ln 1, \ln 2$ (Landauer's 1-bit limit), and $\ln 3$ at different points in the phase diagrams. The T-S diagram vs gate voltage shows thermodynamic state transitions and enables the definition of heat cycles. The results thereby provide a single particle analog to macroscopic T-S diagrams in magnetic, liquid-vapor, and superconducting systems.

[1] H. Leff and A. F. Rex, *Maxwell's Demon 2: Entropy, Classical and Quantum Information, Computing* (CRC, Boca Raton, FL, 2002).

[2] J. C. Maxwell and P. Pesic, *Theory of Heat* (Courier, Mineola, NY, 2001).

[3] L. Szilard, On the decrease of entropy in a thermodynamic system by the intervention of intelligent beings, Behav. Sci. **9**, 301 (1964).

[4] R. Landauer, Irreversibility and heat generation in the computing process, IBM J. Res. Dev. **5**, 183 (1961).

[5] W. H. Zurek, Maxwell's demon, Szilard's engine and quantum measurements, in *Frontiers of Nonequilibrium Statistical Physics* (Springer, New York, 1986), pp. 151–161.

[6] J. V. Koski, V. F. Maisi, J. P. Pekola, and D. V. Averin, Experimental realization of a Szilard engine with a single electron, Proc. Natl. Acad. Sci. USA **111**, 13786 (2014).

[7] J. M. Parrondo, J. M. Horowitz, and T. Sagawa, Thermodynamics of information, Nat. Phys. **11**, 131 (2015).

[8] J. P. Pekola, Towards quantum thermodynamics in electronic circuits, Nat. Phys. **11**, 118 (2015).

[9] K. Chida, S. Desai, K. Nishiguchi, and A. Fujiwara, Power generator driven by Maxwell's Demon, Nat. Commun. **8**, 15301 (2017).

[10] J. V. Koski and J. P. Pekola, Maxwell's demons realized in electronic circuits, C. R. Phys. **17**, 1130 (2016).

[11] A. Aydin, A. Sisman, and R. Kosloff, Landauer's principle in a quantum Szilard engine without Maxwell's Demon, Entropy **22**, 294 (2020).

[12] S. Zozor, G. M. Bosyk, and M. Portesi, On a generalized entropic uncertainty relation in the case of the qubit, J. Phys. A: Math. Theor. **46**, 465301 (2013).

[13] J. P. Pekola and I. M. Khaymovich, Thermodynamics in single-electron circuits and superconducting qubits, Annu. Rev. Condens. Matter Phys. **10**, 193 (2019).

[14] K. Ono, S. N. Shevchenko, T. Mori, S. Moriyama, and F. Nori, Analog of a Quantum Heat Engine Using a Single-Spin Qubit, Phys. Rev. Lett. **125**, 166802 (2020).

[15] K. Xu, J.-J. Chen, Y. Zeng, Y.-R. Zhang, C. Song, W. Liu, Q. Guo, P. Zhang, D. Xu, H. Deng, K. Huang, H. Wang, X. Zhu, D. Zheng, and H. Fan, Emulating Many-Body Localization with a Superconducting Quantum Processor, Phys. Rev. Lett. **120**, 050507 (2018).

[16] Z. A. K. Durrani, *Single-Electron Devices and Circuits in Silicon* (World Scientific, Singapore, 2009).

[17] L. P. Kouwenhoven, C. M. Marcus, P. L. McEuen, S. Tarucha, R. M. Westervelt, and N. S. Wingreen, Electron transport in quantum dots, in *Mesoscopic Electron Transport* (Springer, New York, 1997), pp. 105–214.

[18] K. K. Likharev, Single-electron devices and their applications, Proc. IEEE **87**, 606 (1999).

[19] W. G. Van der Wiel, S. De Franceschi, J. M. Elzerman, T. Fujisawa, S. Tarucha, and L. P. Kouwenhoven, Electron transport through double quantum dots, Rev. Mod. Phys. **75**, 1 (2002).

[20] F. Abualnaja, W. He, M. Jones, and Z. Durrani, Device fabrication for investigating Maxwell's Demon at room-temperature using double quantum dot transistors in silicon, Micro Nano Eng. **14**, 100114 (2022).

[21] Z. Durrani, F. Abualnaja, and M. Jones, Room temperature Szilard cycle and entropy exchange at the Landauer limit in a dopant atom double quantum dot silicon transistor, J. Phys. D: Appl. Phys. **55**, 285304 (2022).

[22] M. R. Galpin, D. E. Logan, and H. R. Krishnamurthy, Quantum Phase Transition in Capacitively Coupled Double Quantum Dots, Phys. Rev. Lett. **94**, 186406 (2005).

[23] D. V. Averin, M. Möttönen, and J. P. Pekola, Maxwell's demon based on a single-electron pump, Phys. Rev. B **84**, 245448 (2011).

[24] M. Esposito, R. Kawai, K. Lindenberg, and C. Van den Broeck, Quantum-dot Carnot engine at maximum power, Phys. Rev. E **81**, 041106 (2010).

[25] R. Kosloff and A. Levy, Quantum heat engines and refrigerators: Continuous devices, Annu. Rev. Phys. Chem. **65**, 365 (2014).

[26] M. Josefsson, A. Svilans, A. M. Burke, E. A. Hoffmann, S. Fahlvik, C. Thelander, M. Leijnse, and H. Linke, A quantum-dot heat engine operating close to the thermodynamic efficiency limits, Nat. Nanotechnol. **13**, 920 (2018).

[27] J. C. Gehrig, M. Penedo, M. Parschau, J. Schwenk, M. A. Marioni, E. W. Hudson, and H. J. Hug, Surface single-molecule dynamics controlled by entropy at low temperatures, Nat. Commun. **8**, 14404 (2017).

[28] Y. Wang, Z. Tang, H.-Y. Chen, W. Wang, N. Tao, and H. Wang, Single-molecule calorimeter and free energy landscape, Proc. Natl. Acad. Sci. USA **118**, e2104598118 (2021).

[29] K. Nishiguchi, K. Chida, and A. Fujiwara, Single-electron manipulation in an attofarad-capacitor DRAM, ECS Trans. **104**, 33 (2021).

[30] R. T. Balmer, *Modern Engineering Thermodynamics: Textbook with Tables Booklet* (Academic, New York, 2011).

[31] M. J. Moran, H. N. Shapiro, D. D. Boettner, and M. B. Bailey, *Fundamentals of Engineering Thermodynamics* (Wiley, New York, 2010).

[32] F. Abualnaja, C. Wang, V.-P. Veigang-Radulescu, J. Griffiths, A. Andreev, M. Jones, and Z. Durrani, Room-Temperature Measurement of Electrostatically Coupled, Dopant-Atom Double Quantum Dots in Point-Contact Transistors, Phys. Rev. Appl. **12**, 064050 (2019).

[33] M. K. M. Kirihara, K. N. N. Nakazato, and M. W. M. Wagner, Hybrid circuit simulator including a model for single electron tunneling devices, Jpn. J. Appl. Phys. **38**, 2028 (1999).

[34] P. D. de Réotier, A. Yaouanc, Y. Chapuis, S. H. Curnoe, B. Grenier, E. Ressouche, C. Marin, J. Lago, C. Baines, and S. R. Giblin, Magnetic order, magnetic correlations, and spin dynamics in the pyrochlore antiferromagnet $Er_2Ti_2O_7$, Phys. Rev. B **86**, 104424 (2012).

[35] J. F. Niven, M. B. Johnson, A. Bourque, P. J. Murray, D. D. James, H. A. Dabkowska, B. D. Gaulin, and M. A. White, Magnetic phase transitions and magnetic entropy in the *XY* antiferromagnetic pyrochlores $(Er_{1-x}Y_x)_2Ti_2O_7$, Proc. R. Soc. A **470**, 20140387 (2014).

[36] D. E. Laughlin, Magnetic transformations and phase diagrams, Metall. Mater. Trans. A **50**, 2555 (2019).

[37] Z. Durrani, M. Jones, F. Abualnaja, C. Wang, M. Kaestner, S. Lenk, C. Lenk, I. W. Rangelow, and A. Andreev, Room-temperature single dopant atom quantum dot transistors in silicon, formed by field-emission scanning probe lithography, J. Appl. Phys. **124**, 144502 (2018).

[38] Z. A. Durrani, M. E. Jones, C. Wang, D. Liu, and J. Griffiths, Excited states and quantum confinement in room temperature few nanometre scale silicon single electron transistors, Nanotechnology **28**, 125208 (2017).

[39] See Supplemental Material at http://link.aps.org/supplemental/10.1103/PhysRevResearch.5.033025 for a detailed discussion regarding the effect of gate capacitance ratios.

[40] L. Haar, *NBS/NRC Steam Tables* (CRC, Boca Raton, FL, 1984).